**Thermomechanically Active Electrodes Power Work-Dense Soft Actuators** 

Angel Martinez, Arul Clement, Junfeng Gao, Julia Kocherzat, Mohsen Tabrizi and M. Ravi

Shankar\*

Department of Industrial Engineering

Swanson School of Engineering

University of Pittsburgh, PA 15261

Abstract

The effect of chain extender structure and composition on the thermomechanical properties of

liquid crystal elastomers (LCE) synthesized using thiol-acrylate Michael addition is presented. The

intrinsic molecular stiffness of the thiol chain extender and its relative molar ratio to acrylate-based

host mesogens determine the magnitudes of the thermomechanical strains, temperatures at which

they are realized and the mechanical work-content. A non-linear structure-property relationship

emerges, wherein higher concentrations of flexible extenders first magnify the thermomechanical

sensitivity, but a continued increase leads to weaker actuation. Understanding this interplay leads

to a composite material platform, enabling a peak specific work production of ~2 J/kg using ~115

mW of electrical power supplied at 2 V. Composites of LCE with eGaIn liquid metal (LM) are

prepared, which act as heaters, while being capable of actuation themselves. The

thermomechanically active electrodes convert the electrical power into Joule heat, which they

efficiently couple with the neat LCE to which they are bound. This system harnesses the nascent

responsiveness of the LCE using electrodes that work with them, instead of fighting against them

(or passively standing in the way). Specific work generated increases when subjected to increasing

levels of load, reaching a peak at loads ~260x the actuator weight. These ideas are extended to tri-

\* ravishm@pitt.edu

1

layered actuators, where LCE films with orthogonal molecular orientations sandwich LCE-LM composite heaters. Torsional actuation modes are harnessed to twist under load.

## 1. Introduction

Macromolecular networks composed of orientationally ordered segments have long held the promise of work-generating "material machines" <sup>1, 2</sup>. Liquid crystalline elastomers (LCE) that harness heat or light to drive order-disorder transitions can generate strain responses that are scalable to 10's of percent <sup>3</sup>. Thermotropic responses of LCE produce work density that is comparable to that of natural muscle <sup>4</sup>. Harnessing this work content for practical manipulation requires the seamless integration of the driving thermal source with the active LCE. If the actinic heat can be delivered with low-voltage power sources in an efficient manner, LCE actuators can occupy a unique space for driving actuation at low voltages as illustrated in Figure 1a. The field intensity required per unit actuation strain can be diminutive in comparison to existing actuation systems, while simultaneously requiring power that can be supplied by miniaturized sources.

Architectures examined to-date have utilized microfabricated compliant electrodes <sup>5-8</sup>, carbon nanotubes <sup>9</sup> and coated eGaIn liquid metal (LM) heaters <sup>10</sup>. A few Volts applied across cm-scale samples to is sufficient to generate 10's% strain, while producing volumetric work-density that is in the range of 0.01 - 0.1 J/cm<sup>3</sup>. The idea is to harness Joule heating from electrodes that power the actuation but provide negligible mechanical constraint that stands in the way of the LCE's response. Even in slender LCE actuators (<< mm thick and ~ cm<sup>2</sup> in lateral dimensions), these approaches have proven to be power hungry. The temperature rise, typically above the ambient, required to drive actuation has typically ranged from 70-100 °C. Even, if such Joule heating can be accomplished with low voltage power sources (say < 5 V), power requirements exceed several hundred milli-Watts <sup>6,8</sup>. The likely reason for this is the inefficient thermal coupling between the active material and the Joule heating elements.

Composites of LCE with LM have been explored, where suspended networks of LM droplets act as Joule heaters that are integral within the structure. The compliant LM does not offer mechanical constraint to actuation. However, since some of the active material is replaced by the LM, the work content is traded off in proportion to the LM content required to create the conductive composite <sup>11</sup>. Surprisingly, these actuators have also proven to be power hungry, requiring electrical input at the Watt-scale to manifest the characteristic large strain contractile actuation <sup>12</sup>. If optimized LCEintegrated architectures can be harnessed at input powers an order of magnitude lower, opportunities for actuation platforms relying on frugal power sources can emerge. For example, soft actuators that draw ~100 mW from conventional, miniaturized Li-ion/Li-polymer batteries become feasible for niches such as haptic interfaces on portable electronics, untethered microrobotics, reconfigurable interfaces on flexible electronics and polymeric micromechanical systems. The feasibility of low-profile work-dense LCE actuator modules also enable their seamless integration with both displacement, force and power-magnification mechanisms. Moonie <sup>13, 14</sup> and "Piezo-bow" <sup>15</sup> mechanisms that have traditionally utilized piezoelectric actuators can be harnessed here. Furthermore, latch mechanisms that have been driven using shape memory alloys can harness LCE actuators without loss of generality to enable biomimetic microrobots <sup>16, 17</sup>.

Here, we delineate the material property trade-space of LCE resulting from thiol-acrylate Michael addition between mesogenic (acrylate-based) monomers and dithiol spacers with various structural characteristics/rigidities and mole fractions to reveal compositions that enable work-dense actuation at low actuation temperatures. During these characterizations, we discover a highly non-linear behavior, where increasing molecular flexibility and the increasing ratio of the flexible chain extenders first improve and then degrade the thermomechanical responsiveness. A material

property space emerges, parameterized by the composition, which presents an array of thermal windows of actuation and the realizable work-density. Optimizing a material platform from this trade-space provides a pathway for work-dense actuators that can be powered from ~100 mW electrical sources. The materials are harnessed in the synthesis of responsive LCE-LM composites that integrally bond to neat LCE to which they transmit the Joule heat and with whom they collaboratively deform. The idea to use LCE-LM composites not just as actuators by themselves, but also as heat sources that deform/actuate collaboratively with neat LCEs to utilize the thermal energy more efficiently. The LCE-LM composites are envisioned as active electrodes that transport heat into the neat LCE and harness its work content to the fullest. We show actuation at an order-of-magnitude lower electrical power requirement than that in prior demonstrations. This material architecture also allows for creation of hierarchical architectures, which can harness torsional actuation modes. LCE-LM electrodes sandwiched between two orthogonally patterned LCE films are used to demonstrate the twisted actuation mode that is reminiscent of that observed with twisted nematic LCEs.

# 2. Experimental

Liquid crystal monomers, 1,4-bis-[4-(6-acryloyloxhexyloxy) benzoyloxy]-2 methylbenzene (RM82) were purchased from Wilshire Technologies, Inc. The vinyl cross-linker, 1,3,5-Triallyl-1,3,5-triazine-2,4,6(1H,3H,5H)-trione (TATATO) and radical inhibitor butylated hydroxytoluene (BHT) were purchased from Sigma-Aldrich. The thiol chain extenders 2,2'-(ethylenedioxy) diethanethiol (EDDT), 1,4 benzenedimethanethiol (BDMT) and 4,4'-Bis(mercaptomethyl)biphenyl (BMBP) were purchased from Sigma-Aldrich and Glycol Di(3-mercaptopropionate) (GDMP) was purchased from TCI chemicals. Also, see Figure 1b. The base-catalyst Triethylamine (TEA) was

also purchased from TCI chemicals. These materials were used to explore the material response space in which the material composition is the parameter. Irgacure 369 was used as the photoinitiator and was acquired from CIBA specialty chemicals.

## 2.1. LCE Synthesis:

Liquid crystal elastomers (LCEs) were synthesized via a thiol-acrylate Michael addition reaction. LCE networks were prepared starting with three monomers: RM82 (diacrylate liquid crystal monomer) and thiol (SH, spacer monomer) for the first network and vinyl (cross-linker monomer) for the second network. The synthesis route pioneered by Yakacki<sup>18</sup> was adapted here for the range of compositions. The LCEs investigated in this work were prepared at various concentrations of spacer monomers (thiol), while the molar ratio of RM82 (1.0 mol) to the cross-linker (0.3 mol) was kept constant in all the samples. The thiol spacer:RM82 mole ratios were 1.0, 1.2 and 1.4 mol for EDDT, BDMT and BMBP, and 0.8, 1.0, and 1.2 mol for GDMP. The thiol was added to the diacrylate RM82 monomer and then heated to 120 °C for a few seconds to melt the sample. While melted, the samples were mixed with a rotary mixer for a few seconds just prior to adding the cross-linker, 2 wt. % of BHT, 2 wt. % of the photo-initiator (I-369) and 2 drops of TEA (Et<sub>3</sub>N). This uncured LCE mixture was filled into a prepared cell, which is constructed with clean glass substrates, as described below.

The glass substrates were cleaned by sonication for 20 minutes in a 2% water solution of Alconox cleaner and then rinsed thoroughly using de-ionized water. Subsequently, they were sonicated in isopropanol (IPA) for 20 minutes and dried. We coated the glass substrates with Ease Release 200 (Smooth-On Inc.) for easy removal of the films after their fabrication. 50 µm spacers were placed

at the corners of the glass substrates and the monomer mixture was poured on the surface. Then the second glass substrate was pressed over the mixture to spread it throughout the cell gap, which is set by the spacers. The cell containing the mixture was bound together with binding clips. Once bound, the cell was retained at 80 °C for 30 minutes to induce oligomerization. We lightly cross-linked the sample in the isotropic state with 365 nm UV light at an intensity of 50 mW/cm² (Omni cure, Lumen Dynamics), illuminating for 60 seconds on each side. After this, the cell was split open and the film was recovered and cut into 1 cm (length) by 1.5 cm (width) sheets. Then the films were mounted across a fine translation stage and stretched to 1.65 times their original length. The stretching of the film causes the mesogens to align parallel to the stretching direction. Uniaxially aligned planar samples were thus created. Then, while mechanically maintaining the strain, the film was photo-polymerized at room temperature with 365 nm UV light at an intensity of 50 mW/cm² for 10 minutes to "freeze-in" the alignment.

## 2.2. LCE-LM Composite:

LCEs were synthesized using the procedure described above. Eutectic LM Ga-In alloy was prepared by combining 3:1 weight ratio of Ga and In (Indium Corporation) followed by homogenization at 150 °C. First, a suspension of LM droplets was prepared by combining 2 g of LM and 5 mL of THF via magnetic stirring at 1000 rpm for 15 minutes and then decanting 4 mL of the THF solution. Next, the LM suspension was incorporated into an uncured LCE mixture followed by magnetic stirring for 10 minutes at 1000 rpm. After degassing, this final mixture is ready to integrate with neat LCE films as active heaters in composite actuators.

The uncured LCE-LM mixture is blade-coated onto oligomerized (not yet fully crosslinked) LCE films to create an 80 µm layer. These films are kept under vacuum at room temperature overnight to remove the residual THF. Then, the LCE-LM/LCE bilayer is stretched to 1.65 times its length to induce a uniaxial director alignment in both the LCE-LM composite and the integrated neat LCE. While maintaining the strain, the film is photo-polymerized at room temperature with 365 nm UV light at an intensity of 50 mW/cm² for 10 minutes. Finally, the LCE-LM composite layers were "mechanically sintered" by applying pressure using a roller until the sample was conductive. This process leads to an internally percolating network of LM within the LCE-LM <sup>11</sup>. The conductive composite layer becomes the Joule heater. Two 8-µm-thick copper strips were attached at two opposite ends of the LCE-LM/LCE bi-layer films on the LCE-LM composite side using conductive epoxy. The copper strips are oriented orthogonally to the director and were used to connect to electrical power sources.

To create a tri-layer LCE/LCE-LM/LCE film two 45 μm oligomerized LCE films were used. One of them was blade-coated with an uncured LCE-LM mixture to creating an LCE-LM/LCE bi-layer. The thickness of the LCE-LM coating was 120 μm. Both the individual LCE and the LCE-LM/LCE were aligned and individually processed as outlined above. 8 μm copper connectors were attached to the bi-layer, enable powering of the LCE-LM Joule heater. Then, the neat LCE film was laid on top of the LCE-LM/LCE bi-layer film, so that the directors of the neat LCE and bi-layer films are perpendicular to one another, creating a tri-layer LCE/LCE-LM/LCE film. Essentially, a twisted tri-layer architecture was created as a route for emulating the essential features of a "twisted nematic" film<sup>19, 20</sup>. Finally, the tri-layer was polymerized for 10 minutes

under UV light at an intensity of 50 mW/cm<sup>2</sup>. A strip is then cut from the tri-layer LCE/LCE-LM/LCE composite film at a 45° angle to the stretching direction.

#### 2.3. Characterization of thermomechanical properties:

To benchmark the thermomechanical response of LCE, contractile strain was measured as a function of temperature using 1 cm × 1 cm × 40  $\mu$ m films of various compositions from ambient temperature to 165 °C. A hotplate with a temperature controller and read-out was used to perform these experiments. The samples were decorated with spots using a marker to enable tracking of the displacement. Strains were calculated from the displacement as a function of the temperature. The work content of the actuators was measured by performing experiments where LCE films lift weights against gravity. The maximum displacement of the weights due to actuation was measured against a 10 g weight that was attached using Kapton tapes at the boundaries. The maximum strain ( $\epsilon_{max}$ ) generated against the 0.25 MPa ( $\sigma_{app}$ ) load was used to characterize the volumetric work capacity  $W_V = \sigma_{app} \epsilon_{max}$  (mJ/cm³ or mN/mm²) for various compositions. The mechanically loaded LCE film was set close to a hotplate to receive enough heat for the lifting test. The temperature of the samples was measured using thermocouples.

The Joule heating experiments in the LCE-LM composites were performed by completing the circuit using a voltage-controlled power source. A microcontroller system was created for supplying the power to the actuator and measuring the current drawn as a function of time. The controller was also capable of supplying pulsed power to the actuator modules to examine dynamic actuation profiles using Joule heating. A FLIR 325A infrared camera was used to track the

temperature fields generated in the actuators. Work and strain generation was tracked against loads that were hung from the films. Strain was tracked by tracking markers placed on the actuators.

#### 3. Results and Discussion

The actuation strain as a function of temperature was recorded for the various material systems as illustrated in Figures 2b-e. The strain  $\varepsilon = \frac{L(T)}{L_0} - 1$  is defined with respect to the original length  $L_0$ measured along the nematic director at ambient temperature. L(T) is the length of the sample measured along the nematic director as a function of temperature T. We find that the structure of the dithiol chain extender modulates the thermomechanical window of actuation over a 60 °C range. The actuation can be triggered from < 50 °C to > 110 °C. To characterize the strain response we adopt the strategy used by Finkelmann<sup>21</sup>. The nominal transition temperature  $T_{\rm NI}$  is taken as the steepest point of the thermomechanical strain-temperature curve. This essentially corresponds to the inflection point of the curves, where the thermomechanical sensitivity is the highest. The strain-temperature curves, averaged from three heating experiments, were differentiated. Gaussian fits to the differentiated curves were used to determine the extrema corresponding to the inflection points. From this, Figure 3a illustrates the variation of the  $T_{\rm NI}$  and the work generated ( $W_{\rm V}$ ) against a stress of 0.25 MPa ( $\sigma_{app}$ ) for the various compositions examined here. Also, see Table 1. Recall, that  $W_{\rm V} = \sigma_{\rm app} \varepsilon_{\rm max}$  was measured by characterizing the maximum strain generated by the various samples in the presence of an opposing  $\sigma_{app}$ . Having determined the  $T_{NI}$ , the broadness of the thermomechanical transition window  $\Delta T$  was measured in a manner that again draws from Finkelmann<sup>21</sup>. This was measured from the thermomechanical strain measurements by drawing a tangent line at  $T_{\rm NI}$ . Half of the broadness,  $\Delta T/2$ , is defined between  $T_{\rm NI}$  and the temperature at which the tangent line intersects with the maximum strain  $\varepsilon_{max}$  (inset in Figure 3b). The

thermomechanical sensitivity of the various compositions defined by  $\varepsilon_{\text{max}}/\Delta T$  was plotted against the corresponding  $W_{\text{V}}$  in Figure 3b. From the point of view of materials for effective thermomechanical actuation, those on the bottom right corner of Figure 3a are favorable because they enable actuation at lower activation temperatures ( $T_{\text{NI}}$ ). Similarly, those at the top right corner of Figure 3b are favorable because they are characterized by the steepest strain transition window (thermomechanical sensitivity). Both these regions are also characterized by work-dense actuation.

For a given mole ratio of the chain extender,  $T_{\rm NI}$  shows a trend with GDMP (46 °C) < EDDT (50 °C) < BDMT (73 °C) <BMBP (113 °C). This is for a 1:1 mole ratio between the host mesogens (RM82) and the dithiol chain extender (Table 1). These suggest an effect of the intrinsic molecular rigidity of the dithiols. We quantify the intrinsic rigidity of the chain extenders. This was accomplished by defining the bond flexibility indices of the constituent molecules<sup>22</sup>. We utilize a parameterization that defines the flexibility on a scale of 0-10 by coopting ideas from fuzzy logic theory and builds upon earlier approaches, e.g. Kier's methods<sup>23, 24</sup>. The atomic flexibility ( $\Phi_a$ ) for each atom is calculated. Here, C-sp3 are assigned an index of 10, but this is corrected for by accounting for the masses of the adjoining atoms and normalizing to remain within the 0-10 scale. See Ref. <sup>22</sup> for details of this approach. Within this framework, atoms forming a double or a triple bond and constituting an aromatic ring are assigned a 0.5. The bond flexibility for each bond is defined as the mean of the atomic flexibility of the adjacent atoms:  $\Phi_{bd} = \sum \Phi_a/2$ . The bond flexibilities for those constituting the chain extenders is illustrated in Figure 3c. The average flexibility ( $\Phi_{bd av}$ ) characterizing the molecule is obtained by averaging the flexibilities of the constituent bonds. These values are illustrated in Figure 3c above the structures. This characterization reveals a non-linear trend in the  $T_{\rm NI}$  value for the 1 mole ratio compositions. While EDDT ( $\Phi_{bd_{av}} = 9.25$ ) is characterized by the highest flexibility, GDMP ( $\Phi_{bd_{av}} = 6.0327$ ) shows the lowest  $T_{NI}$  value. This does not imply that further decrease in the molecular flexibility leads to continued decline in the transition temperature. We find that BDMT and BMBP are characterized by lower flexibility, but their  $T_{NI}$  values are higher than that for both GDMP and EDDT. Thus, endowing smaller flexibility in the chain extender first leads to decrease in the  $T_{NI}$ , but this trend reverses with further decrease in the flexibility.

This non-linearity repeats itself when we examine the strain sensitivity and the maximum saturation strain generated for a given dithiol. Figures 2b-e reveal how, for a given chain extender structure, increasing its mole fraction first leads to an increase in the maximum achievable strain. However, continued increase leads to a decline in the strain value. This trend is also reflected in the thermomechanical strain sensitivity as seen in Figure 3b. The steepness of the strain generation  $(\varepsilon_{\text{max}}/\Delta T)$  first increases when the mole fraction is increased and then decreases. This pattern is also followed in the volume specific work content (work density) generated against the load (Wv). While, we have not explored the effect on the mechanical properties of the LCE in a systematic fashion, a limited characterization of just the EDDT-based LCE system was undertaken. Dynamic mechanical analysis revealed the now familiar non-linear trend. Utilizing EDDT in 1.2 mole ratio showed the largest storage modulus  $(2.87 \pm 0.17)$  MPa, followed by EDDT at 1.4 mole ratio (0.94) $\pm$  0.13) MPa and EDDT at 1.0 mole ratio (0.769  $\pm$  0.26) MPa. Thus, controlling the macromolecular network for optimizing the thermomechanical response involves inducing an optimum level of molecular flexibility at an appropriate mole fraction. This is true for both the intrinsic molecular flexibility of the chain extender itself, as well as the mole fraction in which it is introduced amongst the mesogenic host.

While it is customary to define a  $T_{\rm NI}$  in LCE, in reality, they do not fully undergo a nematic to isotropic transition. Crosslinked LCE undergo a nematic to paranematic transition, where some order is retained even at elevated temperatures. This was illustrated by tracking the birefringent behavior of blueprinted LCE, which showed a high temperature paranematic state at 200 °C in an otherwise mechanically unloaded state <sup>25</sup>. Traditionally, the retention of nematic order in LCE has been traced to a linear coupling between an externally applied load and the order parameter, which penalizes the free energy against loss of nematic order. The load is assumed to be parallel to the director <sup>26</sup>. But, given Ref. <sup>25</sup>, the presence of a high temperature paranematic state in crosslinked LCE implies the presence of an internal field that owes its origins to the constraint produced by the crosslinks, which penalizes the loss of nematic order as an external stress would <sup>26</sup>. These have been considered a form of "frozen-in" internal fields that drive supercritical behaviors in LCE <sup>27</sup>. In our materials, these internal fields likely emerged when the samples were crosslinked in the presence of the tensile strain (1.65x elongation) to enforce the uniaxial alignment. The free energy (F) of the liquid crystalline state  $F = \frac{A}{2}(T - T^*)Q^2 - \frac{B}{3}Q^3 + \frac{C}{4}Q^4 - GQ$  can be truncated to the form:  $F = \frac{1}{2}A(T - T^*)Q^2 - GQ$  at temperatures  $> T_{NI}$  by ignoring the higher order terms of the order parameter Q. T\*, A, B and C are the traditional Landau-de Gennes parameters. This formulism is analogous to the scalar nematic mechanical coupling considered by Warner and Terenie $v^{28}$  but with the distinction that G parameterizes the linear coupling of the order parameter to F-a field intrinsic to the crosslinked LCE. G exists even in the absence of an external mechanical load.

We assume that Q is related to the thermomechanical distortion  $\lambda$  of the LCE:  $Q \approx \frac{\lambda^3 - 1}{\lambda^3 + 2}$ . Here, the distortion is defined with respect to the high temperature state of the material;  $\lambda \to 1$  (as the strain approaches  $\varepsilon_{\text{max}}$ ) when  $T >> T_{\text{NI}}$ . Thus, in our experiments  $\lambda = (\varepsilon + 1)/(\varepsilon_{\text{max}} + 1)$ . Also, see inset in Figure 3b. Minimizing F for  $T > T_{NI}$ , we use the experimental strain data to fit for G/Avalues for the various compositions (Table 1). The strain-temperature curves in Figures 2b-e were used to calculate these values. For a given chain extender, we find that the G/A value increases with increasing mole fraction (Table 1). This implies that a greater mole fraction of the chain extender dilutes the mesogenic content and endows a greater flexibility of the chains, but it also penalizes the loss of nematic order. Note, that EDDT is the exception to this rule. In EDDT, G/Aincreases when its mole ratio is increased from 1 to 1.2 (0.047 to 0.066) but saturates when increased further to 1.4. But, in general we observe that with increasing mole fraction of a given spacer, G/A increases and thus, more order is retained in the paranematic state. Given that G is the parameter that penalizes the loss of order, this leads to a weaker thermomechanical sensitivity. Thus, a trade-off emerges. The higher the mole fraction of the chain extender, the greater the flexibility and ability to magnify thermomechanical strains. Simultaneously, however, a penalty builds up through a magnification of the G/A value from an intrinsic field, which fights against these gains and reduces the thermomechanical sensitivity of the LCE. Optimizing this trade-off through composition design and a judicious choice of the chain extender is the key to optimizing the thermomechanical actuation from LCE.

The trade-space of properties accessed in Figures 3a and b led us to choose the GDMP as the chain extender, which is added in a 1:1 mole ratio with the RM82. This material offers a low  $T_{\rm NI}$  of 46 °C and a  $W_{\rm V}$  of 67 mJ/cm<sup>3</sup>. Indeed, BMBP at 1.2 mole ratio offers a higher work density of 75

mJ/cm<sup>3</sup>, but is characterized by a  $T_{\rm NI}$  of 73 °C. We utilize the 1:1 mole ratio of RM82 and GDMP as the platform material to create the LCE-LM electrodes that generate Joule heat but are also intrinsically capable of actuation. The idea is to integrate them with neat LCE, with which they collaboratively actuate to drive work-dense actuation. Figure 4a illustrates the anatomy of the actuator, where the LCE-LM is integrally bound to an LCE. A 80 µm thick LCE-LM electrode is integrated with a 45 µm LCE film forming a bi-layer whose director is aligned along its long-axis. The active length is 1 cm long and is 3 mm along the width. The actuator is 24 mg in weight and is powered using a GW INSTEK (GPS-4303) system that is controlled using a custom-built (Arduino-based) microcontroller. The power supplied to the actuator is directly monitored, while the actuation is imaged using a Celestron (USB microscope) and a FLIR 325A infrared camera. Figure 4b illustrates the time-sequenced images of the sample using visible light and infrared imaging. A 60 s actuation cycle is illustrated using ~115 mW input power by applying a voltage of 2 V across the actuator. A 1 g load ( $F = 10^{-2}$  N; ~48x the mass of the actuator) is hung from the actuator, while it is being tested. The inset infrared images illustrate the progressive development of a temperature field. The apparent heterogeneity in the temperature field revealed by the infrared imaging is likely due to inhomogeneity in the thermal boundary conditions between the clamped end on one side and a hanging mass on the other. Figure 4c tracks the actuation strain calculated along the nematic director against the weight. Discrete points on this curve refer to the deformation states that are illustrated in Figure 4b during the reversible actuation cycle. The strain  $\varepsilon = \frac{L(T)}{L_0} - 1$ is defined with respect to the original length  $L_0$  measured along the nematic director at ambient temperature. After 60 s a peak strain of ~13.5% is reached against the 1 g load, after which the power is turned off. Note, that ~12% is reached in about 10 s, wherein the IR images record a maximum temperature of ~67.9 °C. This temperature is higher than the temperature window

observed in the strain-temperature curves recorded for GDMP 1.0 in the absence of any external load (Figure 2c). It indicates opportunities for further increasing the efficiency of the actuation through improved design and processing of the collaborative electrodes. Inefficiencies still remain to be overcome to improve the electrothermal coupling to achieve more power-frugal actuation. After the power is turned off at 60 s, the actuator recovers the original length after 120 s. The IR images in Figure 4b (insets D-F) illustrate the cool down process, where the temperature fields retreat towards the Cu leads. Figure 4c illustrates the complete recovery of the actuation strains upon cooling. Figure 4d illustrates the Force-Displacement  $(F-\delta)$  characteristic that is measured for a range of forces (F = mg) that act against the actuation. Masses (m) are hung from the actuator, as illustrated in the actuator schematic of Figure 4a, and the displacement ( $\delta$ ) is measured. A surprising effect emerges, where the F- $\delta$  characteristic first increases with increasing load and then retreating towards smaller values, beyond a certain threshold, as shown in the plots of Figures 4d and 4e. We also plot the F- $\delta$  behavior with  $\sim$ 75 mW of input power. The displacements achieved with lower input powers are shifted to lower F- $\delta$  values. But the overall trends are similar. Figure 4e illustrates the specific work generated by the actuators as a function of normalized load (suspended mass divided by mass of the actuator). Peak specific work of ~2 J/kg is realized with stimulation at ~115 mW input power, which compares favorably against that generated with forcemagnifying topological defects at temperatures of ~175 °C in prior demonstrations<sup>25</sup>. Accessing these temperatures would require electrothermal power input manifold higher, if using these compositions, even when exploiting mechanical nonlinearities. The specific work content with ~75 mW input power is ~1 J/kg. In both these cases, we find that the LCE-LM systems manifest their highest specific work content, when actuating against a load that is ~260x their own weight. This is consistent with the upward trending F- $\delta$  characteristic observed in Figure 4d.

Figure 5a illustrates the anatomy of the actuator that is characterized by a tri-layer structure. The LCE-LM/LCE bi-layer in the front is characterized by a nematic director at 45° to the long-axis of the strip. The neat LCE strip on the back, which sandwiches the Cu connector leads, is characterized by a nematic director that is aligned orthogonally to the bilayer. This geometry shares the essential features of that observed in twisted nematic ribbons below a critical width <sup>20</sup>. It is also roughly analogous to the behavior of strips excised from orthogonally stretched sheets that are rigidly bonded <sup>29</sup>. Upon stimulation with ~75 mW of power (1 V input), the actuator without a load twists along its central axis (Figure 5b). Clearly, there is some bending observed because the tri-layer is not entirely symmetric through the thickness. The LCE-LM layer shares the nematic orientation of the LCE in the front and this leads to the bending. The actuator was also loaded with a weight of 3 g and then powered. The series of images in Figure 5c (A-F) illustrate a more modest twist in comparison to the unloaded state. These series of images were tracked to measure the twist that was generated over time, which is plotted in Figure 5d. A 0.6 rad twist is observed. The actuator appears to reach the saturation twist in about 25 s, similar to that observed in Figure 4c. When the power is turned off at 60 s, the actuator untwists and fully recovers. Hierarchically designed LCE/LCE-LM/LCE actuators provide a vehicle for eliciting torsional actuation with frugal electrical power sources.

#### 4. Conclusions:

Molecular flexibility of chain extenders has a non-linear effect on the thermomechanical response of LCE. Increasing the intrinsic molecular flexibility of dithiol extenders first increases the thermomechanical sensitivity, which then decreases. Furthermore, given a chain extender structure, increasing its mole fraction has the same effect: increasing the mole fraction increases the responsiveness, but continued increase degrades the response. Navigating the trade-space of structure-property relationships yields compositions that are capable of actuation at low triggering temperature of 46 °C, while manifesting a work-density of 67 mJ/cm<sup>3</sup>. This material platform is also found to be amenable to the facile creation of composites loaded with Ga-In LM inclusions. The LCE-LM composites are processed to form an electrically percolating system that can generate Joule heat in response to an electrical input. Instead of using such composites as actuators themselves, they are harnessed as active electrodes that heat integrally bonded LCE. Since, heat can diffuse from the LCE-LM to the neat LCE film, a specific work content of ~2 J/kg is retained, even with ~115 mW electrical input. This is comparable to that generated with topological defects in blueprinted LCE at actuation temperatures of ~175 °C. Collaborative electrodes work with the actuation of the LCE to enable this. This platform also allows for the fabrication of tri-layer composites constituting two LCE layers that sandwich the LCE-LM heater. Utilizing an orthogonal orientation between the directors of the LCE layers loosely emulates the behavior observed with twisted nematic LCE and generates torsional actuation.

## Acknowledgement

We acknowledge support from the DARPA SHRIMP Program (HR001119C0046) and the National Science Foundation (1635926).

Table 1: Thermomechanical properties of the various compositions explored here are listed. The composition in the first column contains the name of the chain extender and its mole ratio to that of RM82.  $T_{\rm NI}$  is taken as the temperature corresponding to the steepest thermomechanical response (See Figure 3b inset).  $W_{\rm V}$  is the work density generated against a 0.25 MPa load.  $\varepsilon_{\rm max}/\Delta T$  is the thermomechanical strain sensitivity, which illustrates the steepness of the strain generation per unit temperature rise.  $\Delta T$  is defined in the inset of Figure 3b. G is the coefficient of the linear coupling between the order parameter and the free energy, which penalizes the loss of nematic order. The field frozen-in during crosslinking creates this penalty. A is the conventional coefficient to the quadratic coupling between the order parameter and the free energy within the Landau-de Gennes framework.

Composition	$T_{NI}$ (°C) $\pm 0.5$ °C	$Wv(mJ/cm^3)$	$\epsilon_{\rm max}/\Delta T (1/{\rm ^{o}C})$	G/A
EDDT 1.0	50	27±1	0.013±0.001	0.047
EDDT 1.2	53	56±2	$0.029\pm0.002$	0.066
EDDT 1.4	52	49±0.6	$0.014\pm0.001$	0.066
GDMP 0.8	59	28±4	$0.032\pm0.002$	0.012
GDMP 1.0	46	67±3	$0.075\pm0.007$	0.014
GDMP 1.2	47	60±7	$0.063\pm0.006$	0.029
BDMT 1.0	73	39±2	$0.014\pm0.001$	0.005
BDMT 1.2	62	65±3	0.043±0.004	0.025
BDMT 1.4	68	40±2	0.020±0.001	0.043
BMBP 1.0	113	45±2	0.018±0.001	0.069
BMBP 1.2	73	75±3	0.023±0.001	0.16
BMBP 1.4	97	57±4	0.014±0.001	0.26

Figure 1: a) Joule heated LCEs allow access to work-dense mechanical energy generation at diminutive electric field intensities in comparison to other electromechanical approaches. b) A combinatorial material design space is populated by exploring LCEs created using thiol-acrylate Michael addition between RM82 and various mole ratios of a range of chain extenders.

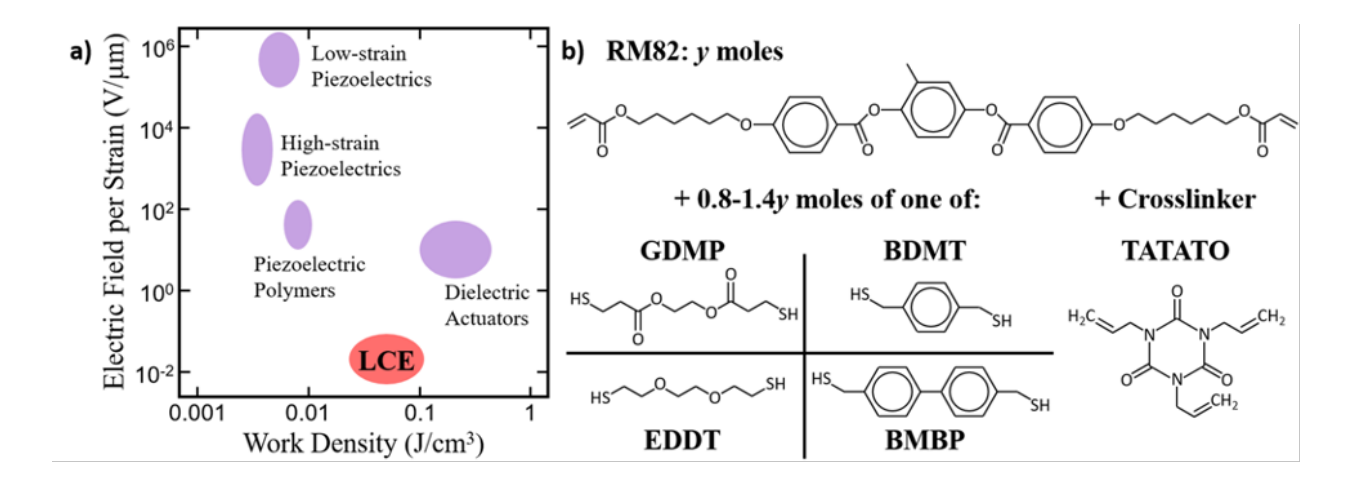


Figure 2: a) Crossed polarized optical images of the planar-oriented monodomain samples is illustrated. The micrographs were acquired with the director orientation parallel and at 45° to the polarizer. Thermomechanical strain response of a sample with EDDT chain extender at 1.2 mole ratio to RM82 is illustrated as a typical example. The sample geometry at 25 °C and 100 °C on a hot plate is shown. Thermomechanical response under load (hanging mass) was used to measure the mechanical work-density that is generated. The black dots were used to track the strain. The experiments were performed for a range of LCE compositions. (b-e) The variation of strain ( $\varepsilon$ ) as a function of temperature without an externally applied mechanical load is plotted.  $\varepsilon = \frac{L(T)}{L_0} - 1$  is defined with respect to the original length  $L_0$  measured along the nematic director at ambient temperature. L(T) is the length of the sample measured along the nematic director as a function of temperature T. b) EDDT in mole ratios of 1, 1.2 and 1.4 with respect to RM82. c) GDMP in mole ratios of 0.8, 1 and 1.2 with respect to RM82. d) BDMT in mole ratios of 1, 1.2 and 1.4 with respect to RM82.

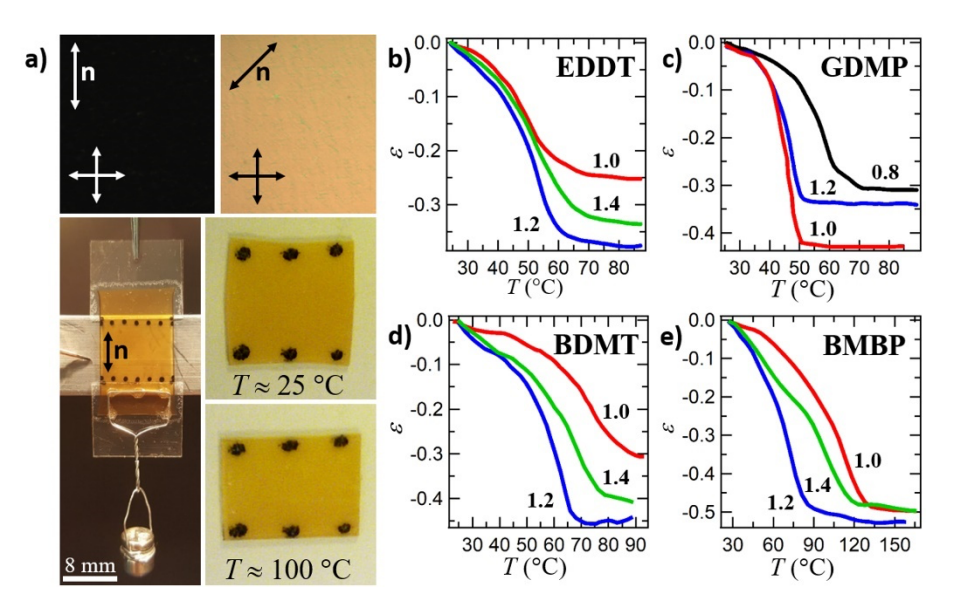


Figure 3: The material property trade space populated with characterizations of various compositions. a) The variation of  $T_{\text{NI}}$  vs Wv. The bottom right corner of the map is the desirable combination of properties. b)  $\varepsilon_{\text{max}}/\Delta T$  vs Wv. The top right corner is desirable. The inset plots the strain generated versus temperature (°C) for the composition with GDMP at a mole ratio of 1 and defines  $T_{\text{NI}}$ ,  $\varepsilon_{\text{max}}$  and  $\Delta T$ . c) The average molecular flexibility ( $\Phi_{\text{bd}\_{\text{av}}}$ ) characterizing the various chain-extenders is given for each.

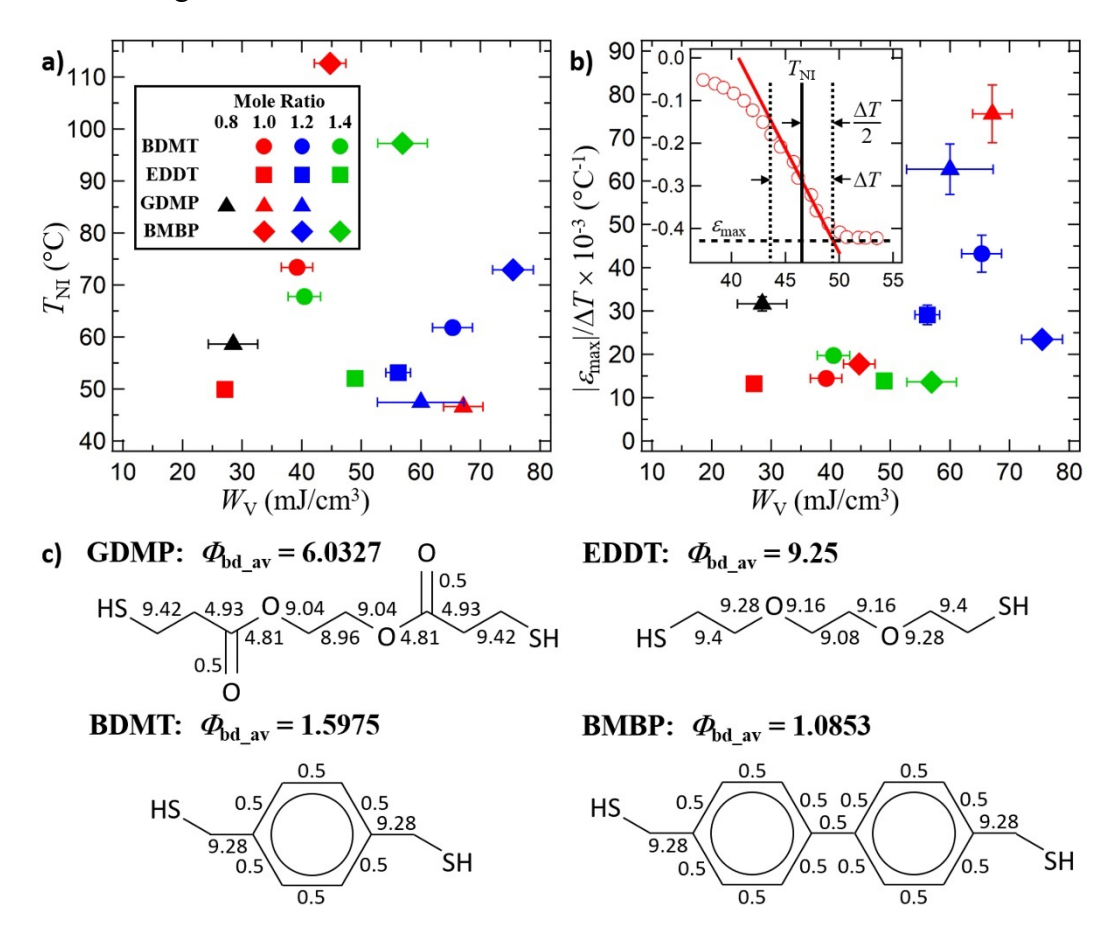


Figure 4: a) A schematic of the anatomy of an actuator. GDMP 1.0 identified from the trade space of material properties is harnessed in LCE-LM composites. These composites are utilized as Joule heaters, which contract collaboratively with the neat LCE sample to which they are integrally attached. **n** illustrates the orientation of the planarly oriented director. b) Time-series images of the sample being actuated with ~115 mW of power supplied from a 2 V source are illustrated. A 1 g load is hung from the actuator. Subpanels A-F illustrate the progressive actuation and relaxation of the actuator. The scale-bar in A is 2 mm. Visible and infra-red images of the actuation are shown. c) The strain (ε) generated by the actuator as a function of time is shown. Data points marked A-F correspond to snapshots in b). d) Force-displacement characteristics are measured to benchmark the performance of the actuators as a function of the load. e) The specific work content (work per mass of the actuator) is measured as a function of the mass of the load normalized per mass of the actuator.

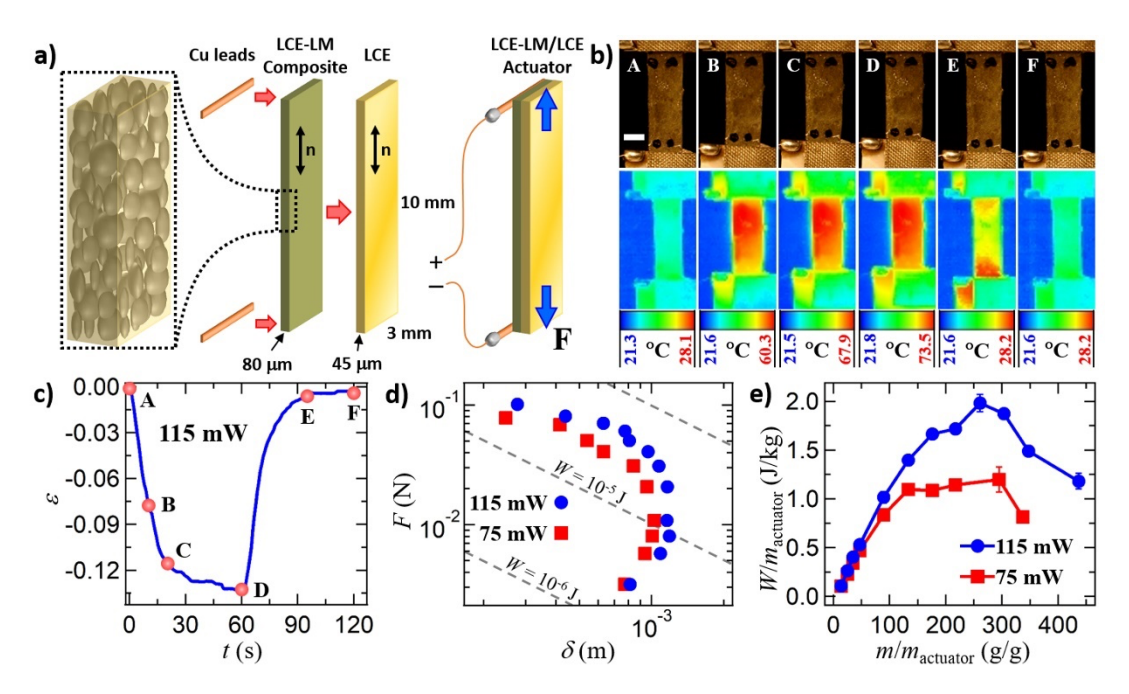
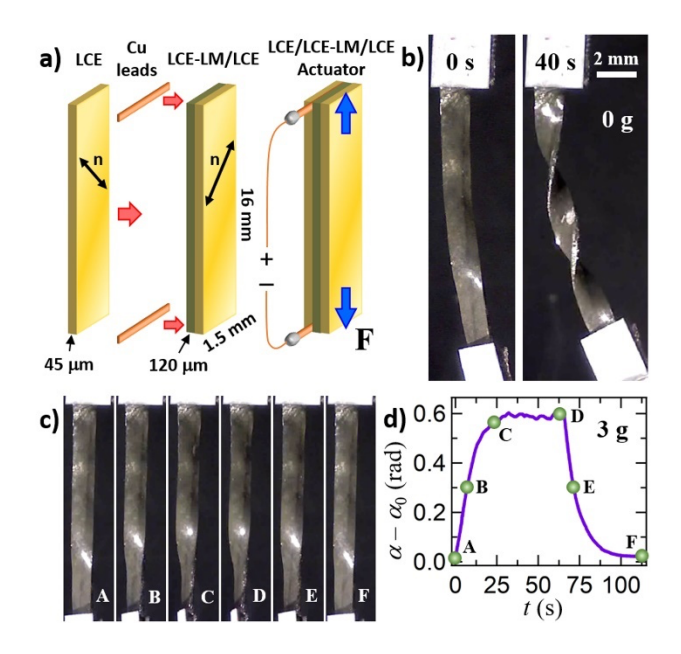


Figure 5: a) Anatomy of the hierarchically structured tri-layer LCE/LCE-LM/LCE actuator is illustrated. The director orientation is orthogonal between the two LCE layers and both are offset with respect to the long axis of the actuator by 45°. The thickness of the LCE-LM coating is 120  $\mu$ m, while that of each of the two LCE layers is 45  $\mu$ m. b) This twisted orientation enables torsional actuation, by the application of Joule heat. The actuator produces a twist of  $\pi$  over its 16 mm length in the absence of a load. c) The actuator is loaded with a 3 g mass at its end and the rotation is tracked as a function of time. A-F illustrates the time-series of images. d) The rotation as a function of time is illustrated for an actuation cycle. A maximum twist of 0.6 rad is produced. The points marked A-F correspond to that in c.



## References

- 1. P.-G. de Gennes, Comptes Rendus de l'Académie des Sciences-Series IIB-Mechanics-Physics-Chemistry-Astronomy, 1997, **324**, 343-348.
- 2. J. M. McCracken, B. R. Donovan and T. J. White, *Advanced Materials*, 2020, **32**, 1906564.
- 3. T. J. White and D. J. Broer, *Nature Materials*, 2015, **14**, 1087-1098.
- J. D. Madden, N. A. Vandesteeg, P. A. Anquetil, P. G. Madden, A. Takshi, R. Z. Pytel, S.
  R. Lafontaine, P. A. Wieringa and I. W. Hunter, *IEEE Journal of Oceanic Engineering*, 2004, 29, 706-728.
- 5. S. Schuhladen, F. Preller, R. Rix, S. Petsch, R. Zentel and H. Zappe, *Advanced Materials*, 2014, **26**, 7247-7251.
- 6. S. Petsch, R. Rix, B. Khatri, S. Schuhladen, P. Müller, R. Zentel and H. Zappe, *Sensors and Actuators A: Physical*, 2015, **231**, 44-51.
- 7. C. Wang, K. Sim, J. Chen, H. Kim, Z. Rao, Y. Li, W. Chen, J. Song, R. Verduzco and C. Yu, *Advanced Materials*, 2018, **30**, 1706695.
- 8. Q. He, Z. Wang, Y. Wang, A. Minori, M. T. Tolley and S. Cai, *Science Advances*, 2019, 5, eaax5746.
- 9. H. Kim, J. A. Lee, C. P. Ambulo, H. B. Lee, S. H. Kim, V. V. Naik, C. S. Haines, A. E. Aliev, R. Ovalle-Robles and R. H. Baughman, *Advanced Functional Materials*, 2019, **29**, 1905063.
- 10. T. A. Kent, M. J. Ford, E. J. Markvicka and C. Majidi, *Multifunctional Materials*, 2020, **3**, 025003.
- 11. M. J. Ford, C. P. Ambulo, T. A. Kent, E. J. Markvicka, C. Pan, J. Malen, T. H. Ware and C. Majidi, *Proceedings of the National Academy of Sciences*, 2019, **116**, 21438-21444.

- 12. F. Michael, M. Palaniswamy, C. P. Ambulo, T. H. Ware and C. Majidi, *Soft Matter*, 2020, **16**, 5878-5885.
- 13. J. D. Ervin and D. Brei, *IEEE/ASME Transactions on Mechatronics*, 1998, **3**, 293-301.
- J. Ueda, T. W. Secord and H. H. Asada, *IEEE/ASME Transactions on Mechatronics*, 2009,
  15, 770-782.
- 15. M. Joshi and S. Priya, *Integrated Ferroelectrics*, 2006, **82**, 25-43.
- 16. J.-S. Koh, S.-P. Jung, M. Noh, S.-W. Kim and K.-J. Cho, *IEEE International Conference on Robotics and Automation*, Karlsruhe, 2013, 26-31.
- J.-S. Koh, E. Yang, G.-P. Jung, S.-P. Jung, J. H. Son, S.-I. Lee, P. G. Jablonski, R. J. Wood,
  H.-Y. Kim and K.-J. Cho, *Science*, 2015, 349, 517-521.
- M. O. Saed, R. H. Volpe, N. A. Traugutt, R. Visvanathan, N. A. Clark and C. M. Yakacki, *Soft Matter*, 2017, 13, 7537-7547.
- 19. K. M. Lee, T. J. Bunning and T. J. White, *Advanced Materials*, 2012, **24**, 2839-2843.
- 20. Y. Sawa, F. Ye, K. Urayama, T. Takigawa, V. Gimenez-Pinto, R. L. Selinger and J. V. Selinger, *Proceedings of the National Academy of Sciences*, 2011, **108**, 6364-6368.
- 21. A. Greve and H. Finkelmann, *Macromolecular Chemistry and Physics*, 2001, **202**, 2926-2946.
- 22. C.-W. von der Lieth, K. Stumpf-Nothof and U. Prior, *Journal of Chemical Information and Computer Sciences*, 1996, **36**, 711-716.
- 23. L. B. Kier, Quantitative Structure-Activity Relationships, 1985, 4, 109-116.
- 24. L. B. Kier, Quantitative Structure-Activity Relationships, 1989, 8, 221-224.
- T. H. Ware, M. E. McConney, J. J. Wie, V. P. Tondiglia and T. J. White, *Science*, 2015,
  347, 982-984.

- 26. J. Schätzle, W. Kaufhold and H. Finkelmann, *Die Makromolekulare Chemie:*Macromolecular Chemistry and Physics, 1989, 190, 3269-3284.
- 27. A. Lebar, Z. Kutnjak, S. Žumer, H. Finkelmann, A. Sánchez-Ferrer and B. Zalar, *Physical Review Letters*, 2005, **94**, 197801.
- 28. M. Warner and E. M. Terentjev, *Liquid Crystal Elastomers*, Oxford university press, 2007.
- 29. S. Armon, E. Efrati, R. Kupferman and E. Sharon, *Science*, 2011, **333**, 1726-1730.